Analysis of the reflection spectra of MAXI J1535-571 in the hard and intermediate states

Yanting Dong [1]★ Zhu Liu,[2] Youli Tuo,[3] James F. Steiner,[4] Mingyu Ge,[3] Javier A. García[5,6] and Xinwu Cao [1,7]★

[1]*Institute for Astronomy, School of Physics, Zhejiang University, 38 Zheda Road, Hangzhou 310027, People's Republic of China*
[2]*Max Planck Institute for Extraterrestrial Physics, Giessenbachstrasse 1, D-85748 Garching, Germany*
[3]*Key Laboratory of Particle Astrophysics, Institute of High Energy Physics, Chinese Academy of Sciences, Beijing 100049, People's Republic of China*
[4]*Harvard-Smithsonian Center for Astrophysics, 60 Garden St Cambridge, MA 02138, USA*
[5]*Cahill Centre for Astronomy and Astrophysics, California Institute of Technology, Pasadena, CA 91125, USA*
[6]*Dr. Karl Remeis-Observatory and Erlangen Centre for Astroparticle Physics, Sternwartstr 7, D-96049 Bamberg, Germany*
[7]*Shanghai Astronomical Observatory, Chinese Academy of Sciences, 80 Nandan Road, Shanghai 200030, People's Republic of China*

ABSTRACT

We report results on the joint-fit of the *NuSTAR* and *HXMT* data for the black hole X-ray binary candidate MAXI J1535-571. The observations were obtained in 2017 when the source evolved through the hard, hard-intermediate, and soft-intermediate states over the rising phase of the outburst. After subtracting continuum components, X-ray reflection signatures are clearly showed in those observations. By modelling the relativistic reflection in detail, we find that the inner radius R_{in} is relatively stable with $R_{in} \lesssim 1.55 R_g$ during the three states, which implies that the inner radius likely extends to the innermost stable circular orbit even in the bright hard state. When adopting $R_{in} = R_{ISCO}$, the spin parameter is constrained to be $0.985^{+0.002}_{-0.004}$ at 90 per cent confidence (statistical only). The best-fitting results reveal that the inclination of the inner accretion disc is $\sim$70–74 deg, which notably conflicts with the apparent orientation of the ballistic jet ($\leq$45 deg). In addition, both the photon index and the electron temperature increase during the transition from hard to soft state. It seems that the corona evolves from dense low-temperature in the low/hard state to tenuous high-temperature after the state transition, which indicates that the state transition is accompanied by the evolution of the coronal properties.

Key words: accretion, accretion discs – black hole physics – methods: data analysis – X-rays: individual: MAXI J1535-571.

1 INTRODUCTION

During a typical outburst of a transient black hole binary, the black hole binary goes through different spectral states with spectral and timing properties changes. As the source luminosity increases, it evolves from the low/hard state (LHS) to the hard and soft intermediate states (HIMS, SIMS), then enters into the high/soft state (HSS, Belloni et al. 2005; Remillard & McClintock 2006). It is generally agreed that the change of spectral states is induced by the evolution of the accretion geometry of the black hole binary system.

In the HSS, the source spectrum is dominated by thermal emission ($\sim$1 keV) accompanied by a hard power-law tail. The accretion flow is composed of an optically thick and geometrically thin accretion disc (Shakura & Sunyaev 1973a) with its inner radius likely at the innermost stable circular orbit (ISCO, Tanaka & Lewin 1995; Steiner et al. 2010). In the LHS, the spectrum is dominated by the hard power-law X-rays, together with the very faint thermal component detected sometimes. The hard X-rays are produced by the inverse-Compton scattering of thermal emission in a region of hot plasma, the so-called corona, and can be well described by power-law with $\Gamma \sim$

1.4–2.1. In the model of Esin, McClintock & Narayan (1997), at a low accretion rate, the disc is truncated before it reaches the ISCO, and an advection-dominated accretion flow, which is evaporated from the accretion disc (Meyer, Liu & Meyer-Hofmeister 2000; Liu et al. 2002; Qiao & Liu 2010), is in the inner region. A disc with a truncated inner radius of several tens to hundreds of R_g (the gravitational radius and calculated by $R_g = GM/c^2$) has indeed been inferred by modelling the disc component of some black hole X-ray binaries (BHXRBs), e.g. XTE J1118+480 (Esin et al. 2001). With this truncated model, the transition from the LHS to the HSS can be well explained by the extending of inner radius down to the ISCO (Plant et al. 2014). This model has also been invoked to explain the positive correlation between the X-ray photon index and the reflection strength (Zdziarski, Lubiński & Smith 1999; Ezhikode et al. 2020; Panagiotou & Walter 2020).

On the other hand, a black hole binary will experience HIMS and SIMS before it enters the HSS. The thermal emission and the hard X-ray emission are both strong, which leads to a softer spectrum than that in LHS. The HIMS–SIMS transition can be very rapid. They are normally distinguished by the differences in their timing properties. For instance, either a type A or a type B quasi-periodic oscillation (QPO) appears in the SIMS, while a type C QPO is often shown in the HIMS. Black hole binary also shows very weak variability in SIMS

★ E-mail: ytd@zju.edu.cn (YD); xwcao@zju.edu.cn (XC)

(Belloni et al. 2005; Belloni 2010). These intermediate states, as the transition states between the LHS and HSS, may provide import clues on the physical driver for state transition, thus it is important to investigate the properties of the accretion flow during the source in the HIMS and SIMS.

In addition to the hard power-law and the thermal emission, the relativistic reflection spectrum is frequently reported (Fabian et al. 1989; García et al. 2014; Plant et al. 2014; Dong et al. 2020a,b; Feng et al. 2022) in the X-ray spectrum of both BHXRBs and active galactic nucleus (AGNs). The reflection spectrum appears when a substantial flux of coronal photons are reflected from the surface of the disc. As a result, this reflected component includes absorption edges, fluorescent lines, and a Compton hump. If the reflection emissions come from the region that is close enough to the black hole, it will be distorted by the relativistic effects, carrying the information of strong fields (Laor 1991). The study of reflection features can provide insights on the inclination, the iron abundance, and the ionization of the disc, as well as the geometry and the electron temperature of the corona. Moreover, the detailed modelling of reflection features is an important tool to measure the inner radius of the disc (García et al. 2015; Sridhar et al. 2020; Xu et al. 2020). If the inner radius is located at the ISCO, the spin of the black hole can then be estimated (Bardeen, Press & Teukolsky 1972). The study of the reflection spectra in different states offers an opportunity to yield important insights on the co-evolution of the disc and corona. Interestingly, in contrast to the theoretical expectation (e.g. Esin et al. 1997; Meyer et al. 2000), it has been suggested that the inner accretion disc is not truncated by modelling the relativistic reflection in the LHS for some sources. For example, the inner radius is found to be very close to the ISCO for Cyg X-1 (Reis, Fabian & Miller 2010; Parker et al. 2015), GX 339-4 (García et al. 2015; Steiner et al. 2017), and MAXI J1820+070 (Buisson et al. 2019). Whether the truncation of the inner disc in LHS and at what phase the truncation appears are still in hot debate in recent years.

MAXI J1535-571 is an X-ray transient discovered in LHS by *MAXI* (Negoro et al. 2017a) and *Swift* (Kennea et al. 2017), on 2017 September 2 (MJD 57999). Its X-ray spectral and timing properties (Negoro et al. 2017b), together with its bright radio signals (Russell et al. 2017), strongly suggest a black hole primary. MAXI J1535-571 was also observed in the optical and infrared bands (Dinçer 2017; Scaringi & ASTR211 Students 2017). Its X-ray spectra started to soften on September 10 (Kennea et al. 2017; Nakahira et al. 2017), followed by the intermediate state which lasted for 2 months (Shidatsu et al. 2017). During the LHS–HIMS–SIMS transitions, low-frequency QPOs were detected (Huang et al. 2018; Stevens et al. 2018; Stiele & Kong 2018; Sreehari et al. 2019), and the evolution of compact jet and relativistic jet were reported (Russell et al. 2019, 2020). Russell et al. (2019) also constrained the jet inclination to be ≤45 deg. The source is heavily absorbed with a line-of-sight (LOS) column density larger than 10^{22} cm^{-1} (Stevens et al. 2018; Cúneo et al. 2020, and the references therein). The source distance (*D*) is estimated to be $4.1^{+0.6}_{-0.5}$ kpc based on the analysis on H I absorption spectrum (Chauhan et al. 2019).

Xu et al. (2018) analysed the *NuSTAR* data observed on September 7 during which MAXI J1535-571 was in the bright phase of the LHS. They found a strong relativistic reflection component in the *NuSTAR* data. They reported no significant disc truncation and a rapidly rotating black hole (>0.84 and >0.987 with the `relxilllpcp` and `relxilllcp` model, respectively). Kong et al. (2020) found the spin was $0.7^{+0.2}_{-0.3}$ with the `relxilllpcp` model using the data obtained by *HXMT*, also on the September 7, but the exposure time was less than 1 ks. Miller et al. (2018) and Sridhar et al. (2019) constrained the
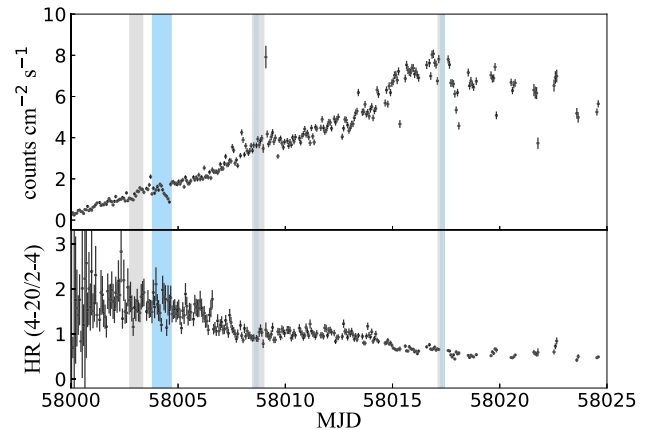

Figure 1. The upper panel shows the *MAXI*/GSC 2–20 keV orbital light curve of the black hole binary MAXI J1535-571. The lower panel shows the *MAXI* hardness ratio which is calculated as the ratio of the counts between 4–20 and 2–4 keV. The blue and grey shaded areas mark the *NuSTAR* and *HXMT* observations analysed in this work, respectively.

spin parameter using *NICER* and *AstroSat* observations, respectively. Both observations were obtained when the source was in the start of the HIMS. The best-fitting model of the *NICER* data indicated a high spin of 0.994 ± 0.002, while *AstroSat* data indicated a moderate spin of $0.67^{+0.16}_{-0.04}$. The inner radius and the spin are degenerate since they both affect the red wing of the fluorescent iron line. So, moderate spin may indicate a moderately truncated disc. The inconsistent values of spin also may attribute to the model difference.

Here, we report a joint analysis of the *NuSTAR* (The Nuclear Spectroscopic Telescope Array, Harrison et al. 2013) and *HXMT* (Hard X-ray Modulation Telescope, or *Insight-HXMT*, Zhang et al. 2014) observations of MAXI J1535-571. We analyse three epochs data obtained as the source increased in intensity while undergoing transition from a bright-hard towards the soft state during the 2017 outburst. *NuSTAR* is the first focusing high-energy X-ray telescope in orbit which covers a broad energy band (3–79 keV) with unprecedented energy resolution and sensitivity in the hard X-ray band. *HXMT*, as the first Chinese X-ray astronomical satellite, includes three slat-collimated instruments: the Low-Energy X-ray Telescope (LE, 1–15 keV), the Medium-Energy X-ray Telescope (ME, 5–30 keV), and the High-Energy X-ray Telescope (HE, 20–250 keV). The data set from both satellites are not affected by photon pile-up effects. Similar spectra analysis of Cyg X-1 (Zhao et al. 2020) and MAXI J1820-070 (Guan et al. 2021; You et al. 2021; Zhao et al. 2021) using *HXMT* has been reported. The paper is organized as follows: in Section 2, we describe the detail of observations and data reduction; the data analysis and results are presented in Section 3; Section 4 includes discussions and Section 5 includes conclusions.

2 OBSERVATIONS AND DATA REDUCTION

We show MAXI J1535-571's light curve and hardness ratio obtained by *MAXI* (Matsuoka et al. 2009) in Fig. 1. In this paper, we analyse three *NuSTAR* observations (blue shadow in Fig. 1) with exposure time of 8685, 2258, and 1531 s, respectively. Quasi-simultaneous *HXMT* observations are also analysed with exposure time of 5614.5, 4316, and 3496 s, respectively. We mark *HXMT* observations as grey shadow in Fig. 1. For the data in Epoch 1 (ObsID: 90301013002), the *NuSTAR* and *HXMT* are not observed simultaneously with the *NuSTAR* observation carried out less than 10 h later than the *HXMT*

Table 1. Details of *NuSTAR* and *HXMT* observations.

Mission	Instrument	ObsID	MJD	Start time	End time	Exposure (s)	Count rate[a] (cts s^{-1})	Total counts[b]	State[c]
				Epoch 1					
NuSTAR	FPMA	90301013002[d]	58003.79	09-07 18:41:09	09-08 17:01:09	8685	648.3 ± 0.3	1.11 × 10^7	LHS
	FPMB	–	–	–	–	9077	601.2 ± 0.3		
HXMT	LE	11453500104	58002.72	09-06 17:11:13	09-06 20:22:09	1047	269.5 ± 0.5	8.13 × 10^6	
	ME	–	–	–	–	1331	266.8 ± 0.5		
	HE	–	–	–	–	1309	645.2 ± 1.6		
	LE	11453500105	58002.85	09-06 20:22:09	09-06 23:33:06	898	280.0 ± 0.6		
	ME	–	–	–	–	1218	274.0 ± 0.5		
	HE	–	–	–	–	1730	652.6 ± 1.3		
	LE	11453500106	58002.98	09-06 23:33:06	09-07 02:43:10	1057	289.6 ± 0.5		
	ME	–	–	–	–	1193	283.2 ± 0.5		
	HE	–	–	–	–	1543	664.6 ± 1.4		
	LE	11453500107[d]	58003.11	09-07 02:43:10	09-07 05:54:06	937	296.4 ± 0.6		
	ME	–	–	–	–	1487	287.5 ± 0.5		
	HE	–	–	–	–	1837	666.2 ± 1.2		
	LE	11453500108	58003.25	09-07 05:54:06	09-07 09:05:03	1676	300.9 ± 0.4		
	ME	–	–	–	–	1960	293.6 ± 0.4		
	HE	–	–	–	–	378	671.9 ± 3.0		
				Epoch 2					
NuSTAR	FPMA	80302309002	58008.55	09-12 13:01:09	09-12 18:26:09	2258	1132.0 ± 0.7	5.05 × 10^6	HIMS
	FPMB	–	–	–	–	2418	1032.0 ± 0.7		
HXMT	LE	11453500144	58008.44	09-12 10:38:15	09-12 13:58:12	1137	979.3 ± 0.9	3.73 × 10^3	
	ME	–	–	–	–	2168	407.6 ± 0.5		
	HE	–	–	–	–	1684	462.3 ± 1.3		
	LE	11453500145	58008.58	09-12 13:58:12	09-13 00:41:28	3179	996.2 ± 0.6		
	ME	–	–	–	–	8202	414.2 ± 0.2		
	HE	–	–	–	–	9329	474.1 ± 0.6		
				Epoch 3					
NuSTAR	FPMA	80302309010	58017.21	09-21 04:51:09	09-21 10:46:09	1531	1818.0 ± 1.1	5.50 × 10^6	SIMS
	FPMB	–	–	–	–	1652	1643.0 ± 1.0		
HXMT	LE	11453500901	58017.10	09-21 02:26:26	09-21 06:00:41	1676	2251.0 ± 1.2	5.93 × 10^3	
	ME	–	–	–	–	2967	399.3 ± 0.4		
	HE	–	–	–	–	2467	326.3 ± 1.2		
	LE	11453500902	58017.25	09-21 06:00:41	09-21 09:21:07	1820	2259.0 ± 1.1		
	ME	–	–	–	–	2780	387.4 ± 0.4		
	HE	–	–	–	–	3697	326.3 ± 0.9		

Notes. [a]The count rate is shown within the energy band of 4.0–79.0 keV for *NuSTAR*/FPMA and FPMB, 2.1–10.0, 10.0–27.0, 27.0–60.0 keV for *HXMT*/LE, ME, and HE, respectively.
[b]The total number of counts are shown for the two modules of *NuSTAR* and the three modules of *HXMT* combined spectra.
[c]Spectral states labelled according to Huang et al. (2018) and Tao et al. (2018).
[d]The *NuSTAR* and *HXMT* observations were analysed by Xu et al. (2018) and Kong et al. (2020), respectively.

observation. However, the *NuSTAR* and *HXMT* data show roughly the same reflection spectral features (iron emission line and Compton hump region), suggesting no significant change in the reflection component; we thus still jointly analyse the *NuSTAR* and *HXMT* data to increase the signal-to-noise ratio. The including of the *HXMT*/LE data enables us to perform spectral analysis down to 2.1 keV, which will be valuable to detect the weak thermal emission in LHS. The details of observations of both satellites can be found in Table 1. The three epoch observations are in LH, HIMS, and SIMS, respectively (Huang et al. 2018; Tao et al. 2018). In the following sections, we describe the observations and data reduction for *NuSTAR* and *HXMT*.

2.1 *NuSTAR* data reduction

The *NuSTAR* data were processed using *NuSTAR* Data Analysis Software (NUSTARDAS v2.0.0) with CALDB v20210524, which are included in HEASOFT v6.28. We created cleaned event files using the NUPIPELINE routine. The count rate exceeds 100 counts s^{-1} in these three observations. Therefore, we set STATUEXPR to be 'STATUS==b0000xxx00xxxx000'. Especially for Obs. 1, we also set saacalc = 2, saamode = strict, and tentacle = NO to remove background flares, which is caused by enhanced solar activity. The X-ray spectra, backgrounds, and instrument responses were generated using NUPRODUCTS. The spectra were extracted from a circular region with radius of 180 arcsec centred on MAXI J1535-571, while backgrounds were extracted from a circular region with radius of 180 arcsec located on the same detector. The spectra were grouped with GRPPHA to have at least 30 counts within an energy bin. We choose the 4–79 keV range for the spectral analysis.

2.2 *HXMT* data reduction

HXMT includes the LE, the ME, and the HE. We carried data reduction following the standard procedures for individual instruments, as the suggestions given by *HXMT* team. The data pipelines and

tools of *HXMT* Data Analysis Software (HXMTDAS) v2.04[1] were used. The *HXMT* spectra were extracted based on the cleaned events files, which were filtered by the good time intervals (GTIs). The GTIs recommended by pipeline are intervals when (1) elevation angle is greater than 10 deg; (2) geomagnetic cut-off rigidities are greater than 8 GeV; (3) satellite is not in South Atlantic Anomaly (SAA) and 300 s intervals near SAA; (4) pointing deviation to the source is less than 0.04 deg. We binned the spectra at least 30 counts within an energy bin. Then, the systematic uncertainties of 0.5 per cent/0.5 per cent/3 per cent were added for LE/ME/HE to account for the instrumental uncertainties[2]. For spectral analysis, we use 2.1–10, 10–27, and 27–60 keV energy band for LE, ME, and HE, respectively. The spectra at higher energies are dominated by the background.

Data in Epoch 1 were split into five continuous observations, and both Epochs 2 and 3 were split into two. We used the following ways to check the spectral variability for all observations within one epoch. For each epoch, we performed a joint-fit with an absorbed power-law model to all spectra within this epoch. A constant multiplication factor was also included to account for the flux fluctuation. The parameters column density, photon index, and normalization were linked among spectra. We find their data to model ratios are highly consistent. Additionally, if the photon index was allowed to be float among different observations, the value of it is consistent within the errors. Therefore, the source spectral shape is not significantly variable within each epoch. The average spectra were created with the ADDASCASPEC tool for each of the three epochs, and were used for the subsequent spectral analysis.

3 SPECTRAL ANALYSIS AND RESULTS

The spectral analysis are performed using XSPEC version 12.11.1 (Arnaud 1996), which is included as part of the HEASOFT v6.28. In all models, a multiplicative constant model is included using the `constant` model to account for the differences in the flux calibration between instruments. This constant is fixed at 1.0 for *NuSTAR*/FPMA, and allowed to vary for *NuSTAR*/FPMB and *HXMT*/LE, ME, and HE, unless otherwise noted. We use the `tbabs` model (Wilms, Allen & McCray 2000) to model the neutral Galactic absorption, with the abundances of Wilms et al. (2000) and the cross-sections of Verner et al. (1996) adopted. All parameter uncertainties are quoted at 90 per cent confidence level for one parameter of interest.

3.1 Fitting spectra individually

We initially jointly fitted the *NuSTAR* and *HXMT* data for each of the three epochs with an absorbed power-law model plus a multitemperature thermal disc (`diskbb`) model (Mitsuda et al. 1984). There is no overlap in the coverage among the three instruments of *HXMT*. We therefore linked the three constant parameters together to prevent the degeneracy between the constant parameters for LE/ME/HE and the photon index Γ of power-law. The remaining parameters

were linked for the *NuSTAR* and *HXMT* data. The iron line region between 4 and 8 keV and Compton hump region between 15 and 45 keV were ignored to avoid potential contribution to the power-law continuum. We note that the residual profiles in the high-energy band for *NuSTAR* and *HXMT* are slightly different for Epoch 1. We find that this could be due to the change of the photon index Γ of the the power-law continuum component between the *NuSTAR* and *HXMT* observations in Epoch 1. Indeed, the residuals for the *NuSTAR* and *HXMT* data are consistent if the photon index Γ is fitted independently for the *NuSTAR* and *HXMT* data. Fig. 2 shows the ratios of the data-to-model for three epochs. It is clear that significant reflection features are revealed in all of three epochs. The profile of the iron line appears to be relatively stable with its red wing extending below ∼5 keV over three epochs, indicating that the inner accretion disc may always be at the ISCO. On the other hand, the flux of the iron line decreases from Epoch 1 to 3 (Fig. 3).

We then replaced the power-law model with a reflection model `relxillCp` (relxill v1.4.3, Dauser et al. 2014; García et al. 2014) to fit the relativistically blurred reflection component in the data. The `relxillCp` model also internally includes a continuum component which is calculated using the Comptonization model `nthcomp` (Zdziarski, Johnson & Magdziarz 1996; Życki, Done & Smith 1999). A distance reflection component, which is generally believed to originate from the reflection of the outer accretion disc, is also added using the model `xillverCp` (García & Kallman 2010). The total model is given by `constant*tbabs(diskbb+relxillCp + xillverCp)` in XSPEC. We fitted each epoch independently with this model.

In order to test the potential evolution of the inner radius of the disc over the rise phase of the outburst, we fixed the spin (a_*) of the black hole at its maximal value 0.998 ($R_{ISCO} = 1.235 R_g$). While the inner radius (R_{in}) of the disc was free in the `relxillCp` model, the outer radius of the disc (R_{out}) was fixed at the default value 400 R_g. We found that the best-fitting value of the iron abundance parameter A_{Fe} was very close to the solar abundance in all the three epochs. We thus fixed A_{Fe} at the solar abundance. The emissivity profile is described by a broken power-law in `relxillCp`, i.e. $\epsilon(r) \propto r^{-q_{in}}$ for $r < R_{br}$ and $\propto r^{-q_{out}}$ for $r > R_{br}$. R_{br} is the break radius, while q_{in} and q_{out} are the index for the inner and outer regions, respectively. Our data, however, cannot constrain all the three parameters simultaneously. We thus used a simple power-law to describe the emissivity profile by linking the value of q_{out} to that of q_{in}. All the other parameters (the inclination angle i, the ionization state logxi, the electron temperature kT_e, and the normalization N_{rel}) in the `relxillCp` are free parameters.

The parameters in the `xillverCp` component were linked to those of `relxillCp` except for the ionization ($\log \xi_{xil}$) and the normalization (N_{xil}) parameters. We initially fixed the $\log \xi_{xil}$ of the `xillverCp` component at zero. Compared with the best-fitting results shown in Table A1, the statistics were degraded by $\Delta \chi^2 = 84.5$, 93.7, and 52.5 for 1 deg of freedom in Epochs 1, 2, and 3, respectively. The case that the distant reflection comes from ionized material is consistent with the previous studies (Xu et al. 2018; Sridhar et al. 2019), in which they reported that the ionization of the outer disc could be high (e.g. $\log \xi_{xil} > 0$) and may be different from the inner disc region. We then set $\log \xi_{xil}$ of the `xillverCp` component independent of that ($\log \xi_{rel}$) of `relxillCp`. The two values of $\log \xi$ are consistent within uncertainty for the Epoch 3, but they are quite distinct for Epochs 1 and 2. Therefore, the two values of $\log \xi$ in the `xillverCp` and `relxillCp` were linked for Epoch 3, while
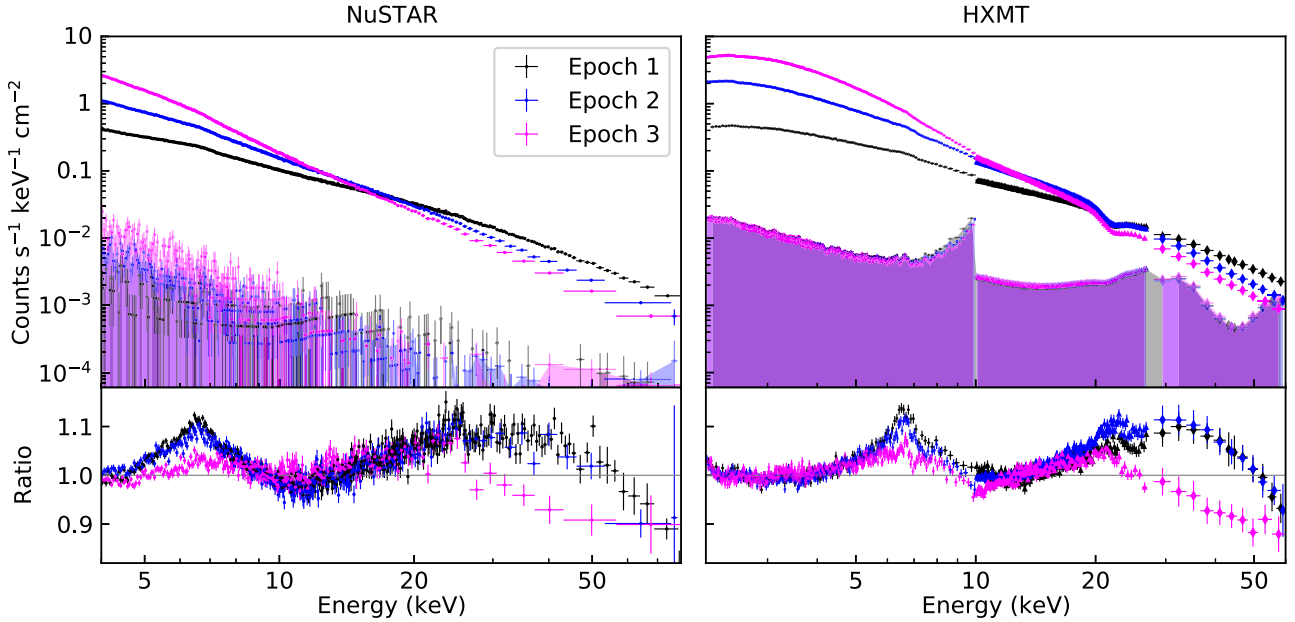
Figure 2. Spectra and ratios of the data-to-model consisting of a multitemperature disc blackbody plus power-law. The *NuSTAR* and *HXMT* spectra were fitted together, but are shown in the left- and right-hand panels, respectively, for clarity. Background spectra using shaded regions are also shown in the upper panels. The spectra were fitted with the energy region 4–8 keV and 15–45 keV ignored. In all panels, Epoch 1 is shown in black, Epoch 2 is shown in blue, and Epoch 3 is shown in magenta. In the right-hand panels, LE, ME, and HE (three instruments of *HXMT*) data are shown in points, triangles, and diamonds. The spectra have been rebinned to higher signal-to-noise in XSPEC for plotting purpose only. The residual structures indicate prominent reflection as seen by the broadened ~6.5 keV Fe line and ~20 keV Compton hump.
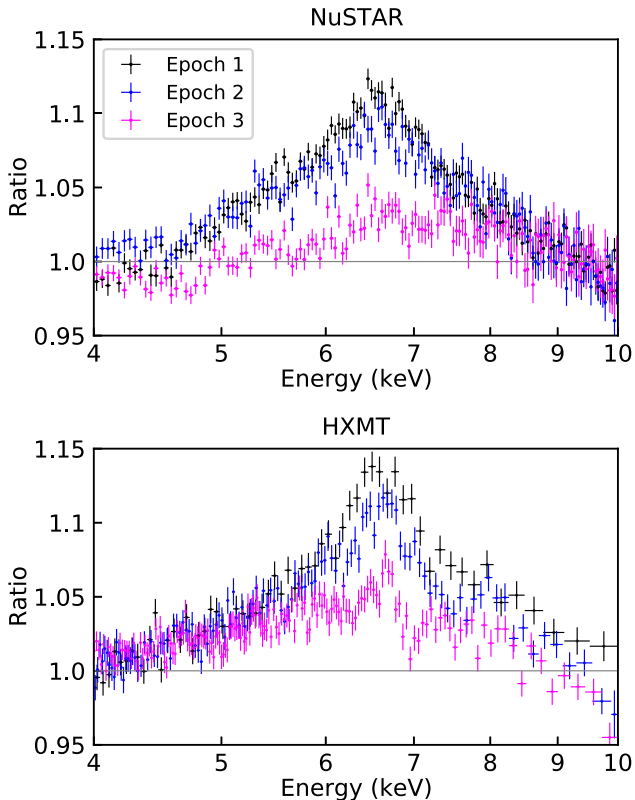

Figure 3. Close-up of iron line profiles in Fig. 2 for the *NuSTAR* and *HXMT* observations. In both panels, Epoch 1 is shown in black, Epoch 2 is shown in blue, and Epoch 3 is shown in magenta. The red wing appears to be relatively stable below ~5 keV during three epochs.

they were fitted independently for Epochs 1 and 2. In addition, we find that unlinking photon index (Γ) of `power-law` between the *NuSTAR* and the *HXMT* data can greatly improve the fitting result for Epoch 1 with $\Delta\chi^2 = 387.52$ for one additional parameter. The values of photon index are constrained to be $1.93^{+0.01}_{-0.02}$ and $1.89^{+0.01}_{-0.02}$, respectively. The minor difference between values of Γ may be attributed to the non-strictly simultaneous observation in Epoch 1.

This model can fit all the three epochs well, yielding reasonable statistics with $\chi^2/\nu = 4576.52/4273 = 1.07$, $3296.6/3323 = 0.99$, and $3317.74/2991 = 1.11$ for the Epochs 1, 2, and 3, respectively. Table A1 presents the details of independent fitting of each epoch. The best-fitting emissivity profile is steep in each of the three epochs, i.e. $q > 9.81$ for Epoch 1, $q = 7.33^{+1.44}_{-0.97}$ for Epoch 2, and $q > 7.22$ for Epoch 3. Xu et al. (2018) also used the same model to fit the *NuSTAR* data of Epoch 1. Our best-fitting results of Epoch 1 are consistent with their results, albeit they fixed q_{out} at 3 with $R_{br} = 10R_g$. Assuming the Newtonian case (Novikov & Thorne 1973; Shakura & Sunyaev 1973b; Reynolds & Begelman 1997), i.e. q was fixed at 3, we got much worse fits with $\Delta\chi^2 = 97.67$, 52.23, and 38,87 for Epochs 1, 2, and 3, respectively.

The inferred LOS hydrogen column density (N_H) varies from ~ 6.95×10^{22} cm^{-1} for Epoch 1 to ~ 5.4×10^{22} cm^{-1} for Epochs 2 and 3. These best-fitting LOS column densities are higher than that expected from Galactic absorption (1.40×10^{22} cm^{-1}), which may imply intrinsic absorption from the source. The variation of this excess absorption could attribute to the wind or the outer region of the disc. However, it can also be due to systematic uncertainty with the model, as such variation of the absorption is not typical in low-mass X-ray binaries. In addition, there is no evidence of the absorption lines detected in the X-ray spectra of MAXI J1535-571. To test whether a constant LOS absorption can fit the data, we performed a simultaneous fit to all the three epochs.

Table 2. Best-fitting parameters to *NuSTAR* and *HXMT* spectra.

Component	Parameter	M1			M2		
		Epoch 1 (LHS)	Epoch 2 (HIMS)	Epoch t (SIMS)	Epoch 1 (LHS)	Epoch 2 (HIMS)	Epoch 3 (SIMS)
`TBabs`	N_H ($\times 10^{22}$ cm^{-2})		$5.48^{+0.05}_{-0.04}$			$5.46^{+0.03}_{-0.02}$	
`diskbb`	T_{in} (keV)	0.324 ± 0.012	$0.349^{+0.013}_{-0.015}$	$1.2^{+0.004}_{-0.008}$	$0.326^{+0.003}_{-0.008}$	$0.34^{+0.006}_{-0.003}$	$1.201^{+0.001}_{-0.002}$
	N_{disc} ($\times 10^3$)	$167.49^{+59.08}_{-42.46}$	$225.27^{+79.51}_{-50.41}$	$1.91^{+0.04}_{-0.03}$	$54.71^{+29.52}_{-13.51}$	$265.76^{+44.03}_{-19.21}$	$1.92^{+0.01}_{-0.02}$
`relxillCp`	q	>9.13	$8.73^{+0.57}_{-0.67}$	>9.5	$7.49^{+0.33}_{-0.41}$	$8.68^{+0.38}_{-0.48}$	>9.72
	a_*		–			$0.985^{+0.002}_{-0.004}$	
	i (deg)		$72.8^{+0.86}_{-1.28}$			$70.7^{+0.17}_{-0.48}$	
	R_{in} (R_g)	$1.51^{+0.04}_{-0.03}$	$1.38^{+0.02}_{-0.03}$	$1.38^{+0.03}_{-0.02}$		–	
	Γ	$1.822^{+0.011}_{-0.023}$	$2.401^{+0.012}_{-0.01}$	$2.795^{+0.006}_{-0.007}$	$1.819^{+0.002}_{-0.003}$	2.401 ± 0.002	$2.79^{+0.002}_{-0.001}$
	$\log\xi_{rel}$ (erg cm s^{-1})	$3.24^{+0.27}_{-0.08}$	3.11 ± 0.06	$3.3^{+0.07}_{-0.05}$	$3.25^{+0.01}_{-0.02}$	$3.13^{+0.03}_{-0.01}$	$3.3^{+0.02}_{-0.03}$
	kT_e (keV)	$18.13^{+0.35}_{-0.29}$	$34.01^{+1.98}_{-2.08}$	>322.3	18.06 ± 0.15	$34.09^{+1.07}_{-1.04}$	>311.01
	R_f	$0.9^{+0.06}_{-0.07}$	$1.08^{+0.12}_{-0.13}$	$0.95^{+0.16}_{-0.09}$	$0.79^{+0.03}_{-0.04}$	0.87 ± 0.06	$0.7^{+0.02}_{-0.05}$
	N_{rel} ($\times 10^{-2}$)	$9.62^{+0.2}_{-1.36}$	$39.88^{+1.05}_{-0.85}$	$134.35^{+1.96}_{-6.28}$	$9.52^{+0.02}_{-0.13}$	$40.68^{+0.08}_{-0.17}$	$134.54^{+0.94}_{-0.46}$
	Γ_{HXMT}	$1.784^{+0.01}_{-0.02}$	–	–	1.78 ± 0.004	–	–
`xillverCp`	$\log\xi_{xil}$ (erg cm s^{-1})	$2.53^{+0.14}_{-0.15}$	$3.66^{+0.14}_{-0.15}$	–	2.8 ± 0.04	$3.58^{+0.08}_{-0.15}$	–
	N_{xil} ($\times 10^{-2}$)	$1.54^{+0.21}_{-0.19}$	$6.58^{+1.7}_{-1.04}$	$16.0^{+4.27}_{-3.82}$	$1.94^{+0.09}_{-0.12}$	$6.23^{+0.6}_{-0.35}$	$17.47^{+2.29}_{-3.26}$
`constant`	C_{FPMB}	1.022 ± 0.001	1.007 ± 0.001	0.997 ± 0.001	1.022 ± 0.001	$1.007^{+0.002}_{-0.001}$	0.997 ± 0.001
	C_{LE}	0.745 ± 0.003	0.955 ± 0.002	0.976 ± 0.001	0.746 ± 0.002	$0.955^{+0.002}_{-0.001}$	0.975 ± 0.001
	C_{ME}	0.741 ± 0.003	0.96 ± 0.002	0.939 ± 0.002	0.741 ± 0.002	0.96 ± 0.002	0.94 ± 0.002
	C_{HE}	0.795 ± 0.012	0.972 ± 0.015	0.955 ± 0.015	$0.795^{+0.012}_{-0.011}$	$0.968^{+0.015}_{-0.014}$	0.947 ± 0.015
	χ^2		11296.6			11356.31	
	ν		10591			10593	
	χ^2_ν		1.07			1.07	

Notes. The model `constant*tbabs(diskbb+relxillCp + xillverCp)` is used to fit in M1 and M2. In M1: the spin parameter a_* is fixed at 0.998, the inner radius R_{in} is free. In M2: a_* is free and linked among three epochs, R_{in} is fixed at -1, which means $R_{in} = R_{ISCO}$. In the two models, the column density N_H and inclination angle i are linked among three epochs. The emissivity profile is assumed to be a single power-law, for which the emissivity index $q_{in} = q_{out} = q$. The constant factor is fixed at unity for *NuSTAR*/FPMA, and free for *NuSTAR*/FPMB (C_{FPMB}), *HXMT*/LE (C_{FPMB}), ME (C_{FPMB}), and HE (C_{FPMB}). The other free parameters listed above: Temperature of the disc (T_{in}); Inner radius of the disc (R_{in}); Photon index (Γ and Γ_{HXMT}, which is only different for Epoch 1); Ionization state ($\log\xi_{rel}$ and $\log\xi_{xil}$ for `relxillcp` and `xillvercp`, respectively, which is linked for Epoch 3); Electron temperature (kT_e); Reflection fraction (R_f); Normalization constants of `diskbb` (N_{disc}), `relxillcp` (N_{rel}) and `xillvercp` (N_{xil}).

3.2 Fitting spectra simultaneously

The LOS column density N_H, inclination angle of the disc i, Fe abundance A_{Fe}, and the black hole spin a_* were not supposed to vary among the three epochs; they were thus linked together. We again fixed A_{Fe} at solar abundance and a_* at the maximum 0.998. The i was left as free parameter. The remaining parameters were fitted independently for each epoch, and were set up as stated in Section 3.1. We refer this model as M1. The model can fit the data well with χ^2/ν = 11296.6/10591 = 1.07. The best-fitting parameters for M1 are presented in Table 2. The components of the model together with the residuals are shown in Fig. 4. A positive feature between 21 and 23 keV in *HXMT* residuals (bottom panels of Fig. 4), which is a known effect that is caused by the photoelectric effect of silver elements (You et al. 2021). Ignoring this energy range (only for the *HXMT*/ME instrument) does not affect the results. We also note that an excess at high-energy tail is shown in the residuals in Epoch 1. Such excess may be attributed to the weaker disc component in the joint-fit, as it is not seen when fit the spectra individually (Section 3.1) of which we got a stronger disc component with also a slightly larger kT_e and higher column density. Since the column density is expected to not vary dramatically among these three epochs, we therefore mainly report on the results from the joint-fit to three epochs (M1).

The best-fitting N_H is found to be $(5.48^{+0.05}_{-0.04}) \times 10^{22}$ cm^{-1}. This high absorption is slightly larger than the result obtained from the *Swift* ($\sim 3.6 \times 10^{22}$ cm^{-1}, Kennea et al. 2017) and *NICER* ($\sim 4.05 \times 10^{22}$ cm^{-1}, Gendreau et al. 2017; $\sim 4.89 \times 10^{22}$ cm^{-1} Miller et al. 2018). It is noteworthy that fixing N_H at a smaller value will significantly worsen the fit, e.g. $\Delta\chi^2 = 186.91$ for 1 deg of freedom if N_H is fixed at 5×10^{22} cm^{-1}.

The best-fitting photon index in Epoch 1 is $\Gamma = 1.822^{+0.011}_{-0.023}$ ($\Gamma = 1.784^{+0.010}_{-0.020}$ for *HXMT* spectra). The best-fitting Γ increases to $2.401^{+0.012}_{-0.010}$ and $2.795^{+0.006}_{-0.007}$ in Epochs 2 and 3, respectively. The temperature of the disc does not change significantly ($\sim$0.3–0.4 keV) in Epochs 1 and 2, while it becomes much higher ($\sim$1.2 keV) in Epoch 3. This trend is clearly illuminated in the top panel of Fig. 4 where we showed the best-fitting model for each component. The relatively weak thermal components showed in Epochs 1 and 2 are comparable, while a prominent thermal component is clearly shown in Epoch 3 (dashed line in the upper panels). We find that a steep emissivity index is required for all the three epochs ($q > 9.13$ for Epoch 1, $q = 8.73^{+0.57}_{-0.67}$ for Epoch 2, and $q > 9.50$ for Epoch 3). The parameter kT_e, which represents the temperature of the electrons in the corona, is constrained to be $18.13^{+0.53}_{-0.29}$ keV for Epoch 1, $34.01^{+1.98}_{-2.08}$ keV for Epoch 2, and >322.30 keV for Epoch 3. The reflection fraction R_f is approximate unity in all three
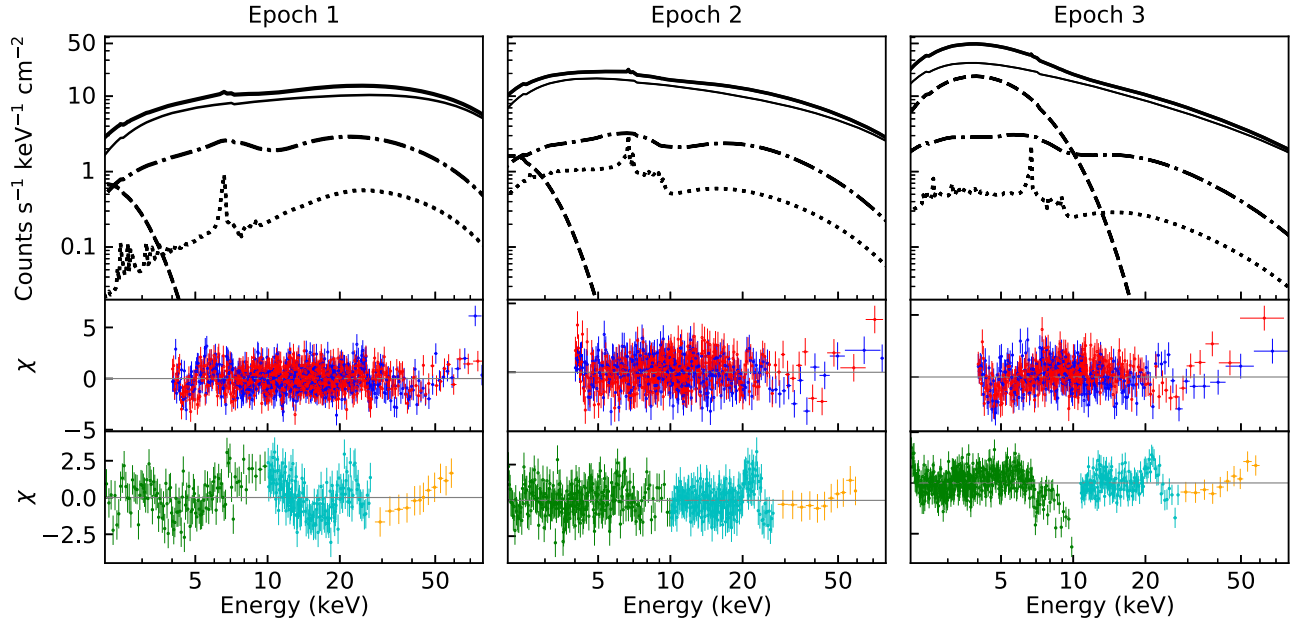
Figure 4. Top panels: the best-fitting models for MAXI J1535-571. We fit three epochs simultaneously, but show the results for each of the epoch in an individual way for clarity. The total model is shown in thick solid line; the thermal emission (`diskbb`) from the disc is shown in dashed line; the Comptonization component `nthcomp` is shown in dot–dashed line, and it is calculated internally by `relxillcp`; the relativistic and distant reflection are shown in dotted and thin solid lines. For Epoch 1, the models for *HXMT* is very similar to that for *NuSTAR*, so only the lines for *NuSTAR* are presented for visual clarity. Middle and bottom panels: *NuSTAR* and *HXMT* residuals with 1σ, respectively. The blue and red are for FPMA and FPMB. The green, cyan, and orange are for LE, ME, and HE, respectively. The data have been rebinned here for display clearly.

epochs, indicating that half of the power-law photons irradiate the disc. The constant factor is low for LE/ME/HE of *HXMT* in Epoch 1, which is because of non-simultaneity. In addition, the inner radius of the accretion disc is broadly consistent among the three epochs with only minor difference, i.e. $R_{in} = 1.51^{+0.04}_{-0.03}$ R_g for Epoch 1, $R_{in} = 1.38^{+0.02}_{-0.03}$ R_g for Epoch 2, and $R_{in} = 1.38^{+0.03}_{-0.02}$ R_g for Epoch 3. However, the best-fitting inclination angle, $i = 72.80^{+0.86}_{-1.28}$ deg, is much higher than that measured from radio jet.

Our results suggest that the inner radius of the accretion disc does not change significantly, which may indicate that it extends to the ISCO in all the three accretion states studied in this work. To self-consistently measure the spin of black hole, we then fixed the inner radius for all three epochs at ISCO ($R_{in} = -1$) in the `relxillcp` model. The a_* was allowed to be free, but linked together among three epochs. We refer this model as M2. Comparing to M1, M2 can equally fit all the data well with $\chi^2/\nu = 11356.31/10593 = 1.07$. We present the best-fitting parameters in Table 2. We obtained a precise measurement of the spin ($a_* = 0.985^{+0.002}_{-0.004}$). The R_f is slightly lower than that in M1. The values of other parameters are similar to those obtained with M1.

We also tried to fit the data with the lamp-post model `relxil-llpcp`. In this scenario, the hard X-ray photons are produced in a point source above the black hole spin axis (Miniutti & Fabian 2004). The height (h) of the corona, instead of q_{in}, q_{out}, and R_{br} in `relxillcp`, is used to describe the illumination of the disc. The lamp-post configuration with a low height of the corona have been successfully used to explain the steep emissivity profile found in several BHXRBs (Duro et al. 2016; García et al. 2018). We jointly fit all the three epoch data together, allowing the height parameter (h) to be vary among the three epochs (the variant of M1). The other parameters set are as M1. This model provides a slightly worse fit to the data comparing with M1, with $\Delta\chi^2 = 163.55$ for the same degree of freedom. The R_{in} cannot be well constrained in the lamp-

post configuration. The obtained R_{in} for Epochs 1, 2, and 3 are < 4.61, < 13.94, and < 8.54 in units of R_g, respectively. The h are estimated to be $37.68^{+7.14}_{-6.11}$, $44.06^{+12.38}_{-6.72}$, and $20.33^{+1.55}_{-1.88}$ in units of R_g for three epochs, respectively, which is not consistent with a compact corona close to the black hole. The inclination angle is $\sim$66–70 deg.

The result presented in Steiner et al. (2017) emphasizes the importance of the Compton scattering of the reflected photons by the hot coronal. To take this effect into account, we built a model in which the model `simpl`, a kernel to calculate the Compton scattering (Steiner et al. 2009), is used to convolve the thermal and reflected photons. In `simpl`, the free parameters are the scattered fraction f_{sc} and the Γ. The f_{sc} represents the proportion of the seed photons being scattered. However, we find that the f_{sc} is poorly constrained. It does not show any significant influence on the calculation of the relativistic reflection. So we opt for M1 instead.

4 DISCUSSIONS

We have presented the detailed multi-epoch analysis of the reflection spectra of the black hole binary candidate MAXI J1535-571 over its rising phase of the outburst in 2017. The data were observed quasi-simultaneously by *NuSTAR* and *HXMT* when the source was in the LHS (Epoch 1), HIMS (Epoch 2), and SIMS (Epoch 3). We initially fitted the three epochs independently. We then performed joint modelling of the data for the three epochs. After subtracting the continuum (absorbed thermal emission plus power-law component), prominent reflection features including the relativistic Fe Kα line and the Compton hump are detected in each of the three epochs. The Fe Kα line profile does not change significantly among the three epochs, while its flux decreases gradually from Epoch 1 to 3. In addition to the smeared reflection from the disc close to the black hole, the distant reflection, which may be reflected from the ionized surface of the outer disc or the companion, was also observed.

The `relxillcp` and `xillvercp` models were used in this work to fit the relativistic and distant reflection, respectively. We found that the hydrogen column density changes when fitted the three epochs independently, which may be induced by the systematic issues. Therefore, we also fitted the data from the three epochs simultaneously with the hydrogen column density assumed to be the same.

The inclination of the accretion disc measured by modelling the X-ray reflection spectra is high (~70 deg) in MAXI J1535-571. This is in agreement with the previous results by fitting *NuSTAR*, *NICER*, and *AstroSat* data in Xu et al. (2018), Miller et al. (2018), and Sridhar et al. (2019), respectively. The inclination we obtained is significantly larger than the jet inclination (≤ 45 deg), which is measured by analysing the radio data (Russell et al. 2019). We also tried to fit the data with the inclination fixed at smaller values, e.g. less than 45 deg. However, this always resulted in an unacceptable fit. Our results imply that the rotation axis of the inner accretion disc seems to be misaligned with the radio jet. Additionally, the jet and binary orbital plane is potentially misaligned. Such discrepancy has been previously reported in other systems like Cyg X-1 (Tomsick et al. 2014; Parker et al. 2015; Walton et al. 2016) and MAXI J1820+070 (Poutanen et al. 2022).

The reflection-based measurements constrained the spin of the black hole in MAXI J1535-571 to be >0.987 (Xu et al. 2018), 0.994 ± 0.002 (Miller et al. 2018), $0.7^{+0.2}_{-0.3}$ (Kong et al. 2020), and $0.67^{+0.16}_{-0.04}$ (Sridhar et al. 2019) by analysing data obtained between September 7 and 13. Because of the strong degeneracy between the spin and the inner radius, the intermediate spin measured in the HIMS by Sridhar et al. (2019) may indicate that the disc is moderately truncated before it extended down to the ISCO. In this work, we use the *NuSTAR* and *HXMT* data observed on September 7 (LHS), 12 (HIMS), and 21 (SIMS) to study the potential evolution of the disc inner radius in MAXI J1535-571. We find that the inner radius does not change significantly in the three epochs with $R_{in} \lesssim 1.55 R_g$. The lack of the disc truncation is inconsistent with the work by Sridhar et al. (2019), which may attribute to the high iron abundance assumed in their model. The phenomenon of the disc inner radius without receding or proceeding represents $R_{in} = R_{ISCO}$. The spin is estimated to be $0.985^{+0.002}_{-0.004}$ via letting a_* free instead of R_{in}, suggesting a rapidly rotating black hole in MAXI J1535-571, which is in agreement with Xu et al. (2018) and Miller et al. (2018).

In addition, we also explored the properties of the thermal emission and the Comptonized component. The parameters related to them present good consistency between M1 and M2. We note that these two components are exhibiting evolution. Epoch 1 is obtained when the source is in the bright phase of the hard state, while Epoch 2 is obtained at the beginning of the hard-to-soft state. In Epoch 3, the luminosity of the source is approaching the peak during the outburst, and the source stay in the soft intermediate state. From Fig. 4, the flux is dominated by the power-law component in Epochs 1 and 2, while the power-law and thermal components are equivalently strong in Epoch 3.

The thermal emission observed above 2.1 keV is equally weak in Epochs 1 and 2, but becomes strong in Epoch 3. As listed in Table 2, the two best-fitting parameters, T_{in} and N_{disc} ($N_{disc} = (r_{in}/D)^2 \times \cos i$),[3] of model `diskbb` change significantly during the source transited from Epoch 2 to 3, which is in agreement with the results in Tao et al. (2018). It appears that the inner radius of the disc is

---

[3]To distinguish from the inner radius R_{in} shown in `relxillcp` model, we use r_{in} to represent the inner radius indicated by `diskbb`.

slightly truncated in Epochs 1 and 2, which is inconsistent with the stable inner radius by modelling relativistic reflection components. Based on the results in Table 2, we calculated the unabsorbed disc flux (0.001–20 keV) for the three epochs, which are ~3.97, ~7.22, and ~8.58 (in units of $\times 10^{-8}$ erg cm^{-2} s^{-1}), respectively. The flux does not show significant change from Epoch 2 to Epoch 3. This is inconsistent with the rise of the count rate shown in Fig. 1, which indicates the increase of the accretion rate. The similar flux of the disc emission may be led by the model without accounting for the Comptonization of the disc photons in corona. On the other hand, the effective temperature and the effective radius should be estimated after correcting the T_{in} and r_{in} by a hardening factor *f*. Because the model `diskbb` does not account for any effects from the general relativity or electron scattering, a positive correlation between *f* and accretion rate was reported in Davis & El-Abd (2019) and Done & Davis (2008). Therefore, the abrupt change in the T_{in} and N_{disc} may be attributed to the change of accretion rate and hardening factor.

The photon index of $\Gamma \sim 1.82$ in Epoch 1 is typical of the hard state. The spectrum softens as the state transition progresses, in Epoch 2 ($\Gamma \sim 2.40$) and Epoch 3 ($\Gamma \sim 2.79$). Γ is used to describe the slope of the power-aw, a component produced by inverse-Compton scatter of the thermal emission in the corona. Γ is related to the electron temperature (kTe) and optical depth (τ) of the corona by formula (Zdziarski et al. 2020):

$$\Gamma = -\frac{1}{2} + \sqrt{\frac{9}{4} + \frac{1}{u\theta(1 + \theta + 3\theta^2)}}, \quad (1)$$

where θ is determined by kTe/m_ec^2, and m_ec^2, the rest mass of the electron, is equal to 511 keV. The term u is the average number of scattering, which is calculated as follows (Zdziarski et al. 2020):

$$u = \tau(a + b\tau) \quad (2)$$

$$a = \frac{1.2}{1 + \theta + 5\theta^2}, b = \frac{0.25}{1 + \theta + 3\theta^2} \quad (3)$$

The corona temperature, however, is challenging to be determined by X-ray spectral analysis because of the low sensitivity of the detectors at high energies (>10 keV), until the launch of the *NuSTAR* mission. Indeed, *NuSTAR* observations have provided opportunities to detect the kTe in a large number of AGNs and X-ray binaries (Lohfink et al. 2015; Pahari et al. 2017; Lanzuisi et al. 2019; Yan, Xie & Zhang 2020). On the other hand, a better statistics can be achieved by adding *HXMT* observations in this work. The values of kTe are constrained to be ~18, ~34, and >311 keV for Epochs 1, 2, and 3, respectively. The unconstrained upper limit in Epoch 3 may be caused by the extremely steep of the power-law and the signal-to-noise ratio is not sufficient enough. The corona temperature changes slightly from Epoch 1 to 2, but increases more than 10 times in Epoch 3.

The increased Γ represents that the spectrum is becoming softer. If it is the case discovered in the LHS, the softening can be explained by the movement of the inner disc towards the black hole or the inflowing corona with a moderately relativistic velocity Zdziarski et al. (1999). More soft photons emitted from the disc will go into the Comptonization region. This will increase the cooling effect of the population of electrons, then the kTe of the corona decreases and the Γ of the power-law increases. In this work, we found that the spectra become softer with steeper power index as the corona temperature increases during the LHS–HIMS–SIMS transition. This is inconsistent with this framework. Moreover, the inner radius has been stable at the ISCO during the three epochs. The behaviour of the
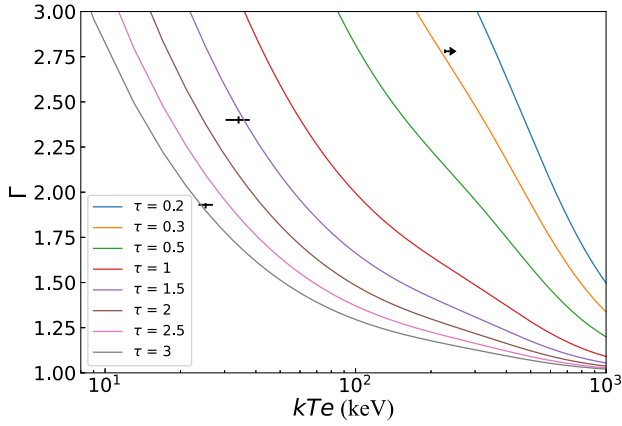
Figure 5. The relationship between Γ and kT_e calculated for the optical depth τ with value range 0.2–3. The black points is quoted from the best-fitting parameters in M1.

Γ and kTe is similar to the behaviour in GX 339-4 (Motta, Belloni & Homan 2009) and GRO 1655-40 (Joinet, Kalemci & Senziani 2008).

Following the above equations, we calculated $\Gamma - kTe$ plane assuming different values of τ (Fig. 5). The optical depth experienced dramatic change. Its value decreased from $\sim$3 (Epoch 1) to $\sim$1.5 (Epoch 2), then to $\sim$0.3 (Epoch 3). It seems that a dense low-temperature corona in the LHS evolves to a tenuous high-temperature corona after the state transition. The low optical depth of the corona in the SIMS may lead to inefficiency of the Compton scatterings in the corona, of which the cooling is substantially suppressed. Therefore, the corona temperature in Epoch 3 becomes much higher. The behaviour seems to imply that the state transition is accompanied by the coronal evolution. The detailed physical mechanism driving such evolution of the corona is beyond the scope of this work.

5 CONCLUSIONS

The black hole candidate MAXI J1535-571 was caught by *NuSTAR* and *HXMT* at three different states during its 2017 outburst: LHS, HIMS, and SIMS. The results of this work on the broad-band reflection spectra by jointly-fit to these three states found that the inner radius of the disc should be stable at the ISCO. The spin $0.985^{+0.002}_{-0.004}$ indicates a fast-rotating black hole in the system. A high inclination angle of the disc is indicated. During the LHS–HIMS transition, the Comptonized component becomes soft, the electron temperature increases slightly, and the thermal component from the disc is relatively comparable. Across the HIMS–SIMS transition, the Comptonized component continues to be soft, the electron temperature shows an abrupt increase, and the thermal component also contributes significantly. We calculated the Γ-kT_e panel giving a range value 0.2–3 of the optical depth τ of the corona. The best-fitting results of Γ and kT_e imply that the τ varies from $\sim$3 to $\sim$1.5, and to $\sim$0.3 over the state transitions. It is clear that the properties of the corona has changed. The corona evolves from dense low-temperature in the LHS to tenuous high-temperature after the state transition, which seems to imply that the physical properties of the corona has changed during the state transition.

ACKNOWLEDGEMENTS

DATA AVAILABILITY

Data used in this article are publicly available from the *NuSTAR* mission (https://heasarc.gsfc.nasa.gov/docs/archive.html) and *HXMT* mission (http://hxmten.ihep.ac.cn).

REFERENCES

Arnaud K. A., 1996, in Jacoby G. H., Barnes J., eds, ASP Conf. Ser. Vol. 101, Astronomical Data Analysis Software and Systems V. Astron. Soc. Pac., San Francisco, p. 17
Bardeen J. M., Press W. H., Teukolsky S. A., 1972, ApJ, 178, 347
Belloni T., Homan J., Casella P., van der Klis M., Nespoli E., Lewin W. H. G., Miller J. M., Méndez M., 2005, A&A, 440, 207
Belloni T. M., 2010, Lecture Notes in Physics, States and Transitions in Black Hole Binaries. Vol. 794, Springer Verlag, Berlin, p. 53
Buisson D. J. K. et al., 2019, MNRAS, 490, 1350
Chauhan J. et al., 2019, MNRAS, 488, L129
Cúneo V. A. et al., 2020, MNRAS, 496, 1001
Dauser T., García J., Parker M. L., Fabian A. C., Wilms J., 2014, MNRAS, 444, L100
Davis S. W., El-Abd S., 2019, ApJ, 874, 23
Dinçer T., 2017, Astron. Telegram, 10716, 1
Done C., Davis S. W., 2008, ApJ, 683, 389
Dong Y., García J. A., Liu Z., Zhao X., Zheng X., Gou L., 2020a, MNRAS, 493, 2178
Dong Y., García J. A., Steiner J. F., Gou L., 2020b, MNRAS, 493, 4409
Duro R. et al., 2016, A&A, 589, A14
Esin A. A., McClintock J. E., Narayan R., 1997, ApJ, 489, 865
Esin A. A., McClintock J. E., Drake J. J., Garcia M. R., Haswell C. A., Hynes R. I., Muno M. P., 2001, ApJ, 555, 483
Ezhikode S. H., Dewangan G. C., Misra R., Philip N. S., 2020, MNRAS, 495, 3373
Fabian A. C., Rees M. J., Stella L., White N. E., 1989, MNRAS, 238, 729
Feng Y. et al., 2022, Sci. China Phys. Mech. Astron., 65, 219512
García J. et al., 2014, ApJ, 782, 76
García J., Kallman T. R., 2010, ApJ, 718, 695
García J. A. et al., 2018, ApJ, 864, 25
García J. A., Steiner J. F., McClintock J. E., Remillard R. A., Grinberg V., Dauser T., 2015, ApJ, 813, 84
Gendreau K. et al., 2017, Astron. Telegram, 10768, 1
Guan J. et al., 2021, MNRAS, 504, 2168
Harrison F. A. et al., 2013, ApJ, 770, 103
Huang Y. et al., 2018, ApJ, 866, 122
Joinet A., Kalemci E., Senziani F., 2008, ApJ, 679, 655
Kennea J. A., Evans P. A., Beardmore A. P., Krimm H. A., Romano P., Yamaoka K., Serino M., Negoro H., 2017, Astron. Telegram, 10700, 1
Kong L. D. et al., 2020, J. High Energy Astrophys., 25, 29
Lanzuisi G. et al., 2019, ApJ, 875, L20
Laor A., 1991, ApJ, 376, 90
Liu B. F., Mineshige S., Meyer F., Meyer-Hofmeister E., Kawaguchi T., 2002, ApJ, 575, 117

Lohfink A. M. et al., 2015, ApJ, 814, 24
Matsuoka M. et al., 2009, PASJ, 61, 999
Meyer F., Liu B. F., Meyer-Hofmeister E., 2000, A&A, 361, 175
Miller J. M. et al., 2018, ApJ, 860, L28
Miniutti G., Fabian A. C., 2004, MNRAS, 349, 1435
Mitsuda K. et al., 1984, PASJ, 36, 741
Motta S., Belloni T., Homan J., 2009, MNRAS, 400, 1603
Nakahira S. et al., 2017, Astron. Telegram, 10729, 1
Negoro H. et al., 2017a, Astron. Telegram, 10699, 1
Negoro H. et al., 2017b, Astron. Telegram, 10708, 1
Novikov I. D., Thorne K. S., 1973, in Dewitt C., Dewitt B. S., eds, Black Holes (Les Astres Occlus). Gordon and Breach, New York, p. 343
Pahari M., McHardy I. M., Mallick L., Dewangan G. C., Misra R., 2017, MNRAS, 470, 3239
Panagiotou C., Walter R., 2020, A&A, 640, A31
Parker M. L. et al., 2015, ApJ, 808, 9
Plant D. S., Fender R. P., Ponti G., Muñoz-Darias T., Coriat M., 2014, MNRAS, 442, 1767
Poutanen J. et al., 2022, Science, 375, 874
Qiao E., Liu B. F., 2010, PASJ, 62, 661
Reis R. C., Fabian A. C., Miller J. M., 2010, MNRAS, 402, 836
Remillard R. A., McClintock J. E., 2006, ARA&A, 44, 49
Reynolds C. S., Begelman M. C., 1997, ApJ, 488, 109
Russell T. D. et al., 2019, ApJ, 883, 198
Russell T. D. et al., 2020, MNRAS, 498, 5772
Russell T. D., Miller-Jones J. C. A., Sivakoff G. R., Tetarenko A. J., Jacpot Xrb Collaboration, 2017, Astron. Telegram, 10711, 1
Scaringi S., ASTR211 Students, 2017, Astron. Telegram, 10702, 1
Shakura N. I., Sunyaev R. A., 1973a, A&A, 24, 337
Shakura N. I., Sunyaev R. A., 1973b, A&A, 24, 337
Shidatsu M. et al., 2017, Astron. Telegram, 11020, 1
Sreehari H., Ravishankar B. T., Iyer N., Agrawal V. K., Katoch T. B., Mandal S., Nandi A., 2019, MNRAS, 487, 928
Sridhar N., Bhattacharyya S., Chandra S., Antia H. M., 2019, MNRAS, 487, 4221
Sridhar N., García J. A., Steiner J. F., Connors R. M. T., Grinberg V., Harrison F. A., 2020, ApJ, 890, 53

Steiner J. F., Narayan R., McClintock J. E., Ebisawa K., 2009, PASP, 121, 1279
Steiner J. F., McClintock J. E., Remillard R. A., Gou L., Yamada S., Narayan R., 2010, ApJ, 718, L117
Steiner J. F., García J. A., Eikmann W., McClintock J. E., Brenneman L. W., Dauser T., Fabian A. C., 2017, ApJ, 836, 119
Stevens A. L. et al., 2018, ApJ, 865, L15
Stiele H., Kong A. K. H., 2018, ApJ, 868, 71
Tanaka Y., Lewin W. H. G., 1995, in X-ray Binaries. Cambridge Univ. Press, Cambridge, p. 126
Tao L. et al., 2018, MNRAS, 480, 4443
Tomsick J. A. et al., 2014, ApJ, 780, 78
Verner D. A., Ferland G. J., Korista K. T., Yakovlev D. G., 1996, ApJ, 465, 487
Walton D. J. et al., 2016, ApJ, 826, 87
Wilms J., Allen A., McCray R., 2000, ApJ, 542, 914
Xu Y. et al., 2018, ApJ, 852, L34
Xu Y., Harrison F. A., Tomsick J. A., Walton D. J., Barret D., García J. A., Hare J., Parker M. L., 2020, ApJ, 893, 30
Yan Z., Xie F.-G., Zhang W., 2020, ApJ, 889, L18
You B. et al., 2021, Nat. Commun., 12, 1025
Zdziarski A. A., Johnson W. N., Magdziarz P., 1996, MNRAS, 283, 193
Zdziarski A. A., Lubiński P., Smith D. A., 1999, MNRAS, 303, L11
Zdziarski A. A., Szanecki M., Poutanen J., Gierliński M., Biernacki P., 2020, MNRAS, 492, 5234
Zhang S., Lu F. J., Zhang S. N., Li T. P., 2014, in Takahashi T., den Herder J.-W. A., Bautz M., eds, Proc.SPIE Conf. Ser. Vol. 9144, Space Telescopes and Instrumentation 2014: Ultraviolet to Gamma Ray. SPIE, Bellingham, p. 914421
Zhao X. et al., 2021, ApJ, 916, 108
Zhao X.-S. et al., 2020, J. High Energy Astrophys., 27, 53
Życki P. T., Done C., Smith D. A., 1999, MNRAS, 309, 561

APPENDIX A: RESULTS FOR INDIVIDUAL FITS TO THREE EPOCHS

Table A1. Best-fitting parameters of individual fits to three epochs.

Component	Parameter	Epoch 1 (LHS)	Epoch 2 (HIMS)	Epoch 3 (SIMS)
`TBabs`	N_H ($\times 10^{22}$ cm^{-2})	$6.95^{+0.18}_{-0.19}$	$5.5^{+0.26}_{-0.24}$	$5.33^{+0.08}_{-0.05}$
`diskbb`	T_{in} (keV)	0.349 ± 0.009	$0.349^{+0.014}_{-0.016}$	$1.215^{+0.006}_{-0.013}$
	N_{disc} ($\times 10^3$)	$213.88^{+41.48}_{-36.03}$	$230.98^{+101.19}_{-71.02}$	1.85 ± 0.04
`relxillCp`	q	>9.81	$7.33^{+1.44}_{-0.97}$	>7.22
	i (deg)	$77.8^{+0.66}_{-0.69}$	$69.69^{+3.07}_{-2.88}$	$68.88^{+5.5}_{-4.08}$
	R_{in} (R_g)	$1.35^{+0.03}_{-0.02}$	1.44 ± 0.06	<1.44
	Γ	$1.927^{+0.014}_{-0.016}$	$2.4^{+0.021}_{-0.02}$	$2.777^{+0.009}_{-0.01}$
	$\log\xi_{rel}$ (erg cm s^{-1})	$2.8^{+0.05}_{-0.04}$	$3.11^{+0.09}_{-0.06}$	$3.32^{+0.2}_{-0.06}$
	kT_e (keV)	$25.2^{+1.75}_{-1.59}$	$34.12^{+3.68}_{-3.84}$	>277.43
	R_f	$1.97^{+0.25}_{-0.27}$	0.89 ± 0.21	$1.14^{+0.24}_{-0.33}$
	N_{rel} ($\times 10^{-2}$)	10.83 ± 0.16	$40.04^{+1.79}_{-1.55}$	$122.11^{+3.16}_{-2.89}$
	Γ_{HXMT}	$1.886^{+0.015}_{-0.016}$	–	–
`xillverCp`	$\log\xi_{xil}$ (erg cm s^{-1})	$2.27^{+0.15}_{-0.09}$	$3.68^{+0.15}_{-0.16}$	–
	N_{xil} ($\times 10^{-2}$)	$1.15^{+0.16}_{-0.15}$	$6.87^{+2.28}_{-1.13}$	$11.88^{+3.32}_{-3.21}$
`constant`	C_{FPMB}	1.022 ± 0.001	$1.007^{+0.002}_{-0.001}$	0.997 ± 0.001
	C_{LE}	0.736 ± 0.002	0.955 ± 0.002	0.976 ± 0.001
	C_{ME}	$0.731^{+0.004}_{-0.003}$	0.96 ± 0.002	0.936 ± 0.002
	C_{HE}	$0.783^{+0.013}_{-0.012}$	0.97 ± 0.015	$0.948^{+0.016}_{-0.015}$
	χ^2	4576.52	3296.6	3317.74
	ν	4273	3323	2991
	χ^2_ν	1.07	0.99	1.11

Notes Fitting three epochs individually with the model `constant*tbabs(diskbb+relxillCp + xillverCp)`. The spin parameter a_* is fixed at 0.998. The inner radius R_{in} is free. The emissivity profile is assumed to be a single power-law, for which the emissivity index $q_{in} = q_{out} = q$. The constant factor is fixed at unity for *NuSTAR*/FPMA, and free for *NuSTAR*/FPMB (C_{FPMB}), *HXMT*/LE (C_{FPMB}), ME (C_{FPMB}), and HE (C_{FPMB}). The other free parameters listed above: Temperature of the disc (T_{in}); Inner radius of the disc (R_{in}); Photon index (Γ for and Γ_{HXMT}, which is only different for Epoch 1); Ionization state ($\log\xi_{rel}$ and $\log\xi_{xil}$ for `relxillcp` and `xillvercp`, respectively, which is linked for Epoch 3); Electron temperature (kT_e); Reflection fraction (R_f); Normalization constants of `diskbb` (N_{disc}), `relxillcp` (N_{rel}), and `xillvercp` (N_{xil}).

This paper has been typeset from a TEX/LATEX file prepared by the author.